CPP

Contributions to Plasma Physics

www.cpp-journal.org

WILEY-VCH

REPRINT

Contrib. Plasma Phys. **53**, No. 10, 796 – 810 (2013) / **DOI** 10.1002/ctpp.201310049

Electron-Ion Relaxation, Phase Transitions, and Surface Nano-Structuring Produced by Ultrashort Laser Pulses in Metals

N. A. Inogamov[1] *, **V. V. Zhakhovsky**[2], **Yu. V. Petrov**[1], **V.A. Khokhlov**[1], **S. I. Ashitkov**[3], **K. V. Khishchenko**[3], **K. P. Migdal**[4], **D. K. Ilnitsky**[4], **Yu. N. Emirov**[5], **P. S. Komarov**[3], **V. V. Shepelev**[6], **C. W. Miller**[2], **I. I. Oleynik**[2], **M. B. Agranat**[3], **A. V. Andriyash**[4], **S. I. Anisimov**[1], and **V. E. Fortov**[3]

[1] Landau Institute for Theoretical Physics, Russian Academy of Sciences, Chernogolovka, Russia
[2] Department of Physics, University of South Florida, Tampa, USA
[3] Joint Institute for High Temperatures, Russian Academy of Sciences, Moscow, Russia
[4] All-Russia Research Institute of Automatics, State Corporation "Rosatom", Moscow, Russia
[5] Advance Materials Research Institute, Florida Intern. University, Miami FL 33174, USA
[6] Institute for Computer Aided Design, Russian Academy of Sciences, Moscow, Russia

Received 12 April 2013, accepted 04 September 2013
Published online 02 December 2013

Key words Laser-matter interaction, phase transitions, surface nano-structuring produced by femtosecond pulses.

Fundamental physical phenomena in metals irradiated by ultrashort laser pulses with absorbed fluences higher than few tens of mJ/cm^2 are investigated. For those fluences, laser-produced electron distribution function relaxes to equilibrium Fermi distribution with electron temperature T_e within a short time of 10-100 fs. Because the electron subsystem has T_e highly exceeding much the ion subsystem temperature T_i the well-known two-temperature hydrodynamic model (2T-HD) is used to evaluate heat propagation associated with hot conductive electron diffusion and electron-ion energy exchange. The model coefficients of electron heat conductivity $\kappa(\rho, T_e, T_i)$ and electron-ion coupling parameter $\alpha(\rho, T_e)$ together with 2T equation of state $E(\rho, T_e, T_i)$ and $P(\rho, T_e, T_i)$ are calculated.
Modeling with 2T-HD code shows transition of electron heat wave from supersonic to subsonic regime of propagation. At the moment of transition the heat wave emits a compression wave moving into the bulk of metal. Nonlinear evolution of the compression wave after its separation from the subsonic heat wave till spallation of rear-side layer of a film is traced in both 2T-HD modeling and molecular dynamics (MD) simulation.
For fluences above some threshold the nucleation of voids in frontal surface layer is initiated by strong tensile wave following the compression wave. If the absorbed fluence is ~ 30 % above the ablation threshold than void nucleation develops quickly to heavily foam the molten metal. Long-term evolution of the metal foam including foam breaking and freezing is simulated. It is shown that surface nano-structures observed in experiments are produced by very fast cooling of surface molten layer followed by recrystallization of supercooled liquid in disintegrating foam having complex geometry. Characteristic lengths of such surface nanostructures, including frozen pikes and bubbles, are of the order of thickness of molten layer formed right after laser irradiation.

1 Introduction

Ultrafast energy deposition on a thin surface layer of a metal target irradiated by ultrashort laser pulse [1] leads to formation of pressure wave [2–10] which eventually breaks to a shock wave during its propagation into the bulk of target [11, 12]. Time required for the wave-breaking is shorter if the relative amplitude P/K of compression wave is higher and if the initial compression wave is steeper; here P is a maximum stress in the compression wave profile and K is the bulk modulus of the metal. Pressure P is approximately proportional to absorbed energy F_{abs}, if P is not too high: $P < K$. At the ablation threshold the pressure in compression wave is $\sim (0.1 - 0.2)K$. In metals the ablation threshold $F_{abs}|_{abl}$ (for absorbed "abs" fluence) is typically in a range $50 - 200$ mJ/cm^2 [9, 11–13]. As an example, $F_{abs}|_{abl} = 65$ mJ/cm^2 has been determined for aluminum in

* Corresponding author. E-mail: nailinogamov@googlemail.com, Phone: +74957029317, Fax: +74957029317

works [14, 15], which has been confirmed in the paper [9]. Another research reported gives 30% higher fluence of $F_{abs}|_{abl} = 90$ mJ/cm^2 [13]. But for refractory metals e.g., Ta, W the threshold $F_{abs}|_{abl}$ is significantly higher than for aluminum. The new (for two-temperature applications) case of tantalum is considered below.

Due to very high-rate deformation, the material response to loading by a laser-generated ultrashort shock wave may remain elastic even for shock pressures approaching to the ultimate strength of solids [10, 16–26]. The mechanism of laser-induced generation of such shock waves in metals is studied in this work by means of two-temperature hydrodynamics (2T-HD) and molecular dynamics (MD) simulation techniques. 2T-HD method includes an effect of electron pressure on material motion [27], and utilizes a model of solid based on quantum density functional theory. We study a sequence of complex processes leading to generation of shock waves, including 2T electron-ion relaxation, propagation of supersonic electron thermal wave, overheating of the solid and ultrafast homogeneous isochoric melting, and pressure build-up in the heated layer.

It is shown that ultrafast deposition of laser energy ~ 100 mJ/cm^2 results in formation of a nonequilibrium two-temperature (2T) state lasting several picoseconds. Due to supersonic propagation of heat into the depth of metal the surface layer of ~ 100 nm thick is heated, where material gains the internal energy of ~ 1 eV/atom and melts quickly. The elastic-plastic transformation and respective structures of elastic-plastic shock waves for different laser intensities are discussed. It is demonstrated that the pressure in an elastic precursor is independent on absorbed energy, but it is coupled with pressure at the melting front.

Expansion of the heated layer leads to strong tensile stress applying to liquid, which triggers nucleation of bubbles followed by foaming of the melt [5, 8, 9, 28–30]. As our simulations indicate, the foam-like material at target surface may expand to a micrometer-sized layer without significant decay of the inter-bubble walls because of the high surface tension of liquid metal. Then the foam begins to collapse, which produces the complex morphology with configurations like bubbles, pikes, mushrooms and other liquid nano-structures. In the meantime the surface temperature drops below the melting point and fast recrystallization initiates freezing of the surface nano-structures. Such nano-structures, including frozen bubbles lying [31–33] beneath the recrystallized metal surface, were found in our experiments and simulations, see discussion below.

2 Two-temperature stage

2.1 Two-temperature equations

System of two-temperature (2T) hydrodynamics equations is

$$\frac{\partial x(x^0,t)}{\partial t} = u(x^0,t), \quad \rho(x^0,t)\frac{\partial x(x^0,t)}{\partial x^0} = \rho^0, \quad \rho^0\frac{\partial u}{\partial t} = -\frac{\partial P(x^0,t)}{\partial x^0}, \tag{1}$$

$$\rho^0\,\frac{\partial (E_e/\rho)}{\partial t} = -\frac{\partial q}{\partial x^0} - \frac{\rho^0}{\rho}\alpha\cdot(T_e - T_i) + \frac{\rho^0}{\rho}\,Q - P_e\frac{\partial u}{\partial x^0}, \quad q = -\frac{\rho\kappa}{\rho^0}\,\frac{\partial T_e}{\partial x^0}, \tag{2}$$

$$\rho^0\,\frac{\partial (E_i/\rho)}{\partial t} = \frac{\rho^0}{\rho}\alpha\cdot(T_e - T_i) - P_i\frac{\partial u}{\partial x^0}, \quad Q = \frac{F_{abs}}{\sqrt{\pi}\,\tau_L\,\delta}\exp\left(-\frac{t^2}{\tau_L^2}\right)\exp\left(-\frac{x}{\delta}\right), \tag{3}$$

where $x - axis$ is perpendicular to the surface of metal film. Q having dimensionality $\mathrm{W/cm^3}$ is a laser energy source term in the electron heat equation (2). Duration of pump laser pulse is τ_L, skin depth is δ, which is a depth of attenuation of incident electromagnetic wave. Time is counted from arrival of the laser pulse maximum to a target surface, while the origin of spatial coordinate x is placed on an initial position of a frontal surface of film.

The unknown functions are: (i) $x(x^0,t)$ giving a lagrangian trajectory of a lagrangian particle in Eq. (1) which was in position x^0 prior to laser pulse arrival; (ii) velocity of this particle $u(x^0,t)$; and (iii) the thermodynamic unknowns. In one-temperature (1T) case there are two thermodynamic unknowns, e.g., density ρ and internal energy E, or density ρ and temperature T. All other thermodynamic functions depend on the chosen two functions. In the 2T case there are three thermodynamic variables, e.g., ρ and electron and ion temperatures T_e and T_i. There are five equations (1-3) for the five unknowns.

2.2 Two-temperature thermodynamics

Equation of 2T state (Eo2TS) includes the internal energy $E(\rho, T_e, T_i)$ and pressure $P(\rho, T_e, T_i)$, which are functions of both electron temperature T_e and ion temperature T_e. The heat conduction coefficient $\kappa(\rho, T_e, T_i)$ and coupling parameter $\alpha(\rho, T_e)$ are also required to solve the system of Eqs. (1-3). Parameter $\alpha(\rho, T_e)$ is practically independent from ion temperature T_i if T_i is higher than Debye temperature θ, which in metals is less or of the order of room temperature. It is shown [27, 34] that this condition is universal for simple (like Al), noble (Au, Cu, Ag, ...), and transition metals (Ni, Fe, Ta, ...).

A new Eo2TS and kinetic coefficients of very refractory metal Tantalum are presented in this work. Functions $E(\rho, T_e, T_i = 0)$ and $P(\rho, T_e, T_i = 0)$ representing Eo2TS are obtained from ab-initio DFT (density functional theory) calculations in the $T_i \to 0$ limit. In DFT calculation of Ta the BCC crystal structure is fixed and density changes as a result of variation of lattice constant. In this approach ions are fixed in their lattice positions at $T_i = 0$. Uniaxial lattice deformations are not considered. Similar works to find Eo2TS have been done previously for nickel [27] and tungsten [35–37]. Non-isotropic lattice deformations such as, e.g., deformations in directions [100], [110], [111], are not considered. Experimental (expr) equilibrium density and lattice constant at the room temperature are: $\rho_0|_{expr} = 16.69$ g/cm^3 and $a_0|_{expr} = 0.33058$ nm.

To find Eo2TS, the two-dimensional plane ρ, T_e is covered by discrete mesh $\rho|_i, T_e|_j$ with small enough mesh size of density $\rho|_{i+1} - \rho|_i$ and electron temperature $T_e|_{j+1} - T_e|_j$. DFT calculations at the mesh nodes $\{\rho|_i, T_e|_j\}$ give pairs of quantities $E|_{i,j}$, and $P|_{i,j}$ representing Eo2TS. Figures 1**a** and 1**b** show the cold pressure curves of Ta obtained by different methods. DFT calculations using generalized gradient approximation (GGA) and local density approximation (LDA) are presented in Fig. 1**a**, together with a cold pressure curve used in equation of state developed for this work (the curve with jump) and a cold pressure curve calculated using Johnson's [38] EAM (embedded atom method) potential (the dashed curve with deep minimum). Johnson's EAM potential overestimates the ultimate tensile strength of Ta. The cold energy curve $E_{cold}(\rho)$ of internal energy per unit volume (i.e. internal energy density) is shown in Fig. 2**a**. It is obtained by integration $\int PdV$ of parabolic approximation of cold pressure curve $P_{cold}(\rho)$ shown in Figs. 1 and 2**a**. The result of integration was converted from energy per unit mass to energy per unit volume $(\int PdV')/V$.

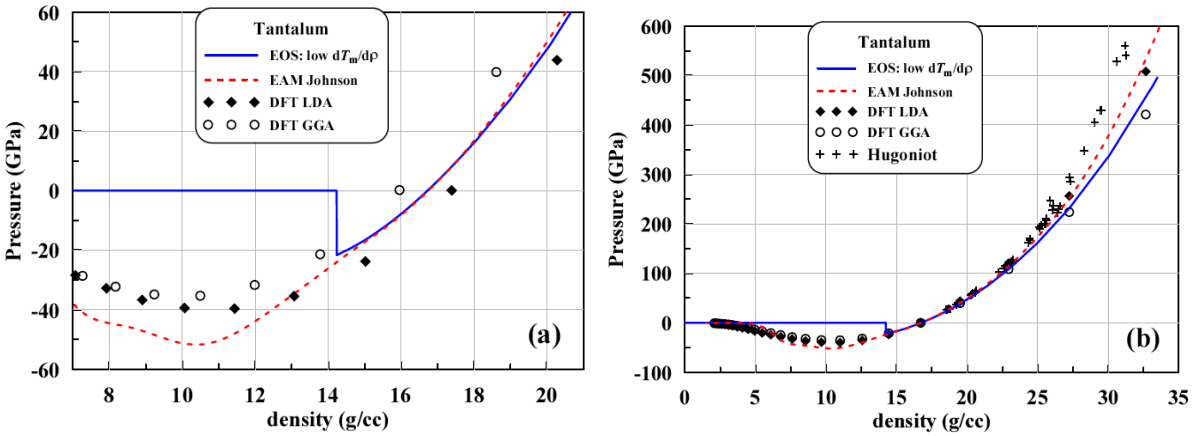

Fig. 1 (a) It is known that DFT simulations (circles, diamonds) determine an equilibrium density $\rho_0|_{DFT}$ with few percents error; LDA is shown by diamonds, GGA - by circles. But DFT results scaled to the experimental density as $\rho \to [(\rho_0|_{expr})/(\rho_0|_{DFT})]\,\rho$ agree well with EOS (Equation of State) for Ta (the blue curve $P_{EOS}(\rho)$) and with Johnson's EAM potential (the red dashed line), as it is demonstrated on the right panel (b). The pressure jump in the function P_{EOS} at expansion ratio $V/V_0 = 1.17$, where $\rho = 14.23$ g/cc and $P = -21.7$ GPa, approximates nucleation of voids and fracture in stretched material. Tensile stress in the nucleation point is 0.6 fraction of the stress in the spinodal "sp" (see Fig. 2a) minimum $\{\rho_{sp} = 10.09\,\mathrm{g/cm^3}; P_{sp} = -36\,\mathrm{GPa}\}$ defined by DFT calculations, expansion ratio the spinodal "sp" to nucleation point is 1.41. (b) The same pressure curves, as in the left panel (a), are plotted up to higher compressions and expansions. They are plotted together with shock Hugoniot [39]. DFT data are scaled to the experimental equilibrium density.

We separate electron contributions, associated with electron excitations, from energy and pressure in cold solid, as it is done in the Mie-Gruneisen approximation of EoS. Energy and pressure of Eo2TS are represented

as sums of cold energy and pressure curves and electron thermal contributions to energy and pressure. The cold curve for energy is shown in Fig. 2a. Electron thermal contributions $E_e(\rho, T_e)$ and $P_e(\rho, T_e)$ are shown as arrows in Fig. 2a. The arrows shift the curves E and P up from the cold curves, because E and P are sums of cold and thermal contributions:

$$E(\rho, T_e, T_i = 0) = E(\rho, T_e = 0, T_i = 0) + E_e(\rho, T_e), \tag{4}$$

$$P(\rho, T_e, T_i = 0) = P(\rho, T_e = 0, T_i = 0) + P_e(\rho, T_e). \tag{5}$$

Here the electron thermal contributions E_e and P_e arise from electron excitations in distinction from the well-known Mie-Gruneisen equation of state where the thermal contributions are from equilibrium single-temperature heating with $T_e = T_i$.

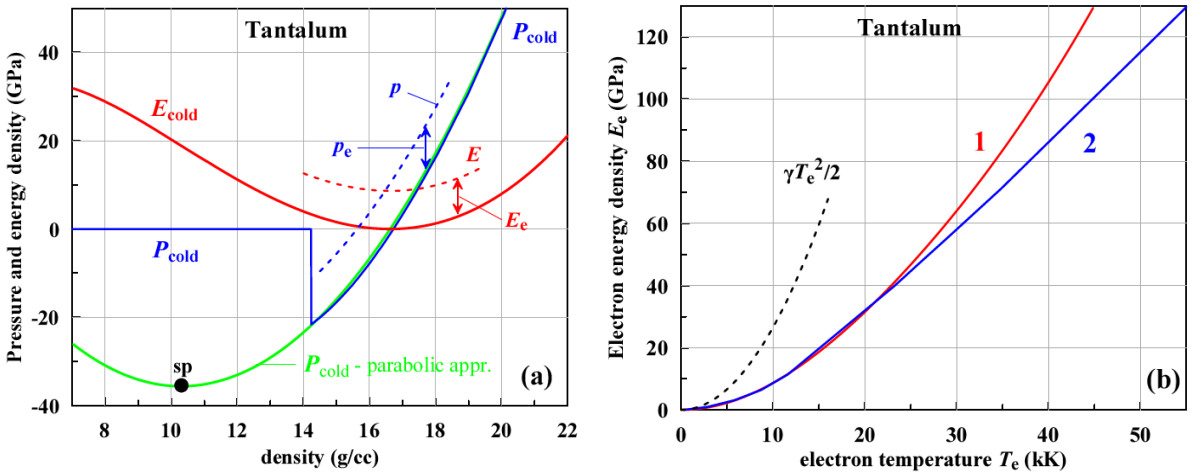

Fig. 2 (a) Pressure and energy density as functions of density. Energy of cold Ta is $E(\rho, T_e = 0, T_i = 0)$ (cold curve E_{cold}). Energy of Ta with cold ion subsystem and with hot electrons is $E(\rho, T_e = 10\,\mathrm{kK}, T_i = 0)$ (dashed curve E); $E = E_{cold} + E_e$ (4). Pressures are $P(\rho, T_e = 0, T_i = 0)$ (cold curve P_{cold}) and $P(\rho, T_e = 10\,\mathrm{kK}, T_i = 0)$ (dashed curve P); $P = P_{cold} + P_e$ (5). Excitation of electrons in fixed specific volume increases energy and pressure. Cold pressure curve $P_{cold}(\rho)|_{EOS}$ with jump (blue curve) is taken from our EOS for Ta. A parabolic approximation of the function $P_{cold}(\rho)|_{EOS}$ is plotted as a green curve. The parabola agrees well with DFT results shown in Fig. 1 and allows us to define the spinodal point "sp" - the minimum of function $P_{cold}(\rho)|_{EOS}$. (b) Fermi free electron model gives dependence $E_e = \gamma T_e^2/2$ shown by dashed line; see also Fig. 3a. The curve 1 has been calculated with DFT code which includes $4f^{14}$ electrons of Ta $4f^{14}\,5d^3\,6s^2$, while the curve 2 has been calculated with DFT code including only the last two electron shells $5d^3\,6s^2$. The curve 1 deviates from the curve 2 with increasing electron temperature T_e as a result of ionization of f-electrons into conduction band.

The shifts E_e and P_e in sums (4,5) increase when electron temperature T_e increases. Corresponding dependencies are shown in Figs. 2b and 3b. DFT calculations with pseudopotential, approximating electrons below the upper two shells $5d^3\,6s^2$, do not allow to include energy loses due to ionization of f-shell. Therefore the curves 1 and 2 in Fig. 2b diverge. In the temperature range shown in Fig. 2b the number of ionized f-electrons is small in comparison with numbers of d- and s-electrons. Appreciable difference between curves 1 and 2 at small ionization degree results from rather large gap of ≈ 15 eV between f- and conducting bands. Ionization leads to increase of the electron heat capacity c_e, as shown in Fig. 3a. It is interesting that the heat capacity c_e saturates not at the value $(3/2)k_B(Z_s + Z_d)$ (total removal of degeneration) but in the intermediate region with the significantly lower value $\sim (3/2)k_B Z_s$. This is particularly evident for such transition metals as Ni or Pt, where number Z_d is large. In an ionization region the electron Gruneisen parameter decreases, and the growth rate of electron pressure P_e with temperature T_e is significantly lower than the growth rate of internal energy E_e, as it is seen in Fig. 3b. The growth rate of $P_e(\rho_0, T_e)$ with T_e decreases since energy added to electron subsystem is mainly consumed for ionization of the f-electrons.

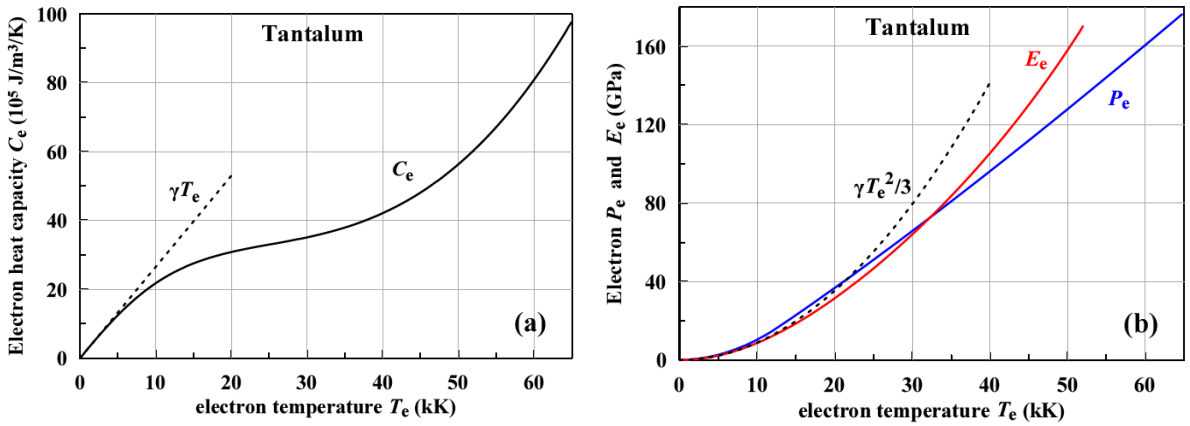

Fig. 3 (a) Three regions in the temperature dependence of electron heat capacity $c_e(\rho_0, T_e) = \partial E_e/\partial T_e|_V$ of Tantalum are: (i) decrease of degeneration degree and approximately linear growth $\gamma = 270$ J/m^3/K^2, (ii) saturation, (iii) new growth due to ionization of f-electrons. The same regions are clearly seen in aluminum and tungsten [36]. (b) Rise of electron pressure P_e with temperature T_e. Function P_e is defined by Eq. (5) and shown in Fig. 2a. The pressure P_e lags behind the electron internal energy E_e as ionization loses come into force. The dashed curve presents Fermi free electron model $P_e = (2/3)E_e$.

For our applications (ablation including 2T effects) it is necessary to consider finite ion temperatures T_i. If $T_i > 0$ then we have

$$E(\rho, T_e, T_i) = E(\rho, T_e = 0, T_i = 0) + E_G(\rho, T_i) + [E_e(\rho, T_e) - E_e(\rho, T_i)], \tag{6}$$

$$P(\rho, T_e, T_i) = P(\rho, T_e = 0, T_i = 0) + P_G(\rho, T_i) + [P_e(\rho, T_e) - P_e(\rho, T_i)] \tag{7}$$

or

$$E(\rho, T_e, T_i) = E(\rho, T_i) + [E_e(\rho, T_e) - E_e(\rho, T_i)], \tag{8}$$

$$P(\rho, T_e, T_i) = P(\rho, T_i) + [P_e(\rho, T_e) - P_e(\rho, T_i)]. \tag{9}$$

In Eqs. (6,7) the functions $E_G(\rho, T_i), P_G(\rho, T_i) = \Gamma E_G(\rho, T_i)$ are Mie-Gruneisen approximations for thermal contributions; $E(\rho, T_e = 0, T_i = 0) = E_{cold}(\rho)$, $P(\rho, T_e = 0, T_i = 0) = P_{cold}(\rho)$ are cold curves. The usual Gruneisen parameter is Γ. In addition to this "ion" parameter Γ, a new "electron" Gruneisen parameter Γ_e appears $P_e(\rho, T_e) = \Gamma_e E_e(\rho, T_e)$. DFT calculations show that the electron parameter $\Gamma_e \approx 1.1$ is smaller than the ion parameter $\Gamma \approx 2$. The Fermi free electron model gives $\Gamma_e = 2/3$. The electron contribution is already included into 1T equation of state where $T_e = T_i$. Therefore, we extract quantities $E_e(\rho, T_i), P_e(\rho, T_i)$ in the second terms of equations (6-9). In our applications the ion temperatures are limited to relatively small amplitude much below the Fermi temperature. For such case the functions $E_e(\rho, T_i)$ and $P_e(\rho, T_i)$ are small.

We write $E_G(\rho, T_i), P_G(\rho, T_i)$ in (6,7) and $E(\rho, T_i), P(\rho, T_i)$ in (8,9). In those expressions, taken from one-temperature (1T) case, we change common (in 1T case) for electrons and ions temperature T to the ion temperature T_i. In condensed phase there are weak dependencies of electron contributions $E_e(\rho, T_e), P_e(\rho, T_e)$ from density ρ. This means that those electron contributions weakly influence the elastic constants. Therefore, the replacement $T \to T_i$ done above means we neglect influence of electron temperature T_e on elastic constants in this approximation. Influence of electron temperature T_e onto elastic constants is important in semiconductors and dielectrics where the weakening of stiffness of solids follows from softening of chemical bonds due to excitation of electrons into conduction bands, see, e.g., [40–42]. This is a reason for non-thermal melting in semiconductors and dielectrics.

From the other hand, some materials demonstrate strengthening of elastic constants with increase of T_e, see Refs. [35, 40, 43]. Below we will neglect possible hardening of metal at high temperatures T_e, which must be relatively small. The replacement $T \to T_i$ allows us to use 1T equation of state to describe ion subsystem. DFT

simulation of energy and pressure for condensed state with excited electron subsystem together with moving ions (MD combined with 2T DFT) is difficult to perform, because it requires a dense 3D mesh in $\{\rho, T_e, T_i\}$ space.

Analytical approximations of electron contributions (4,5) introduced above and shown in Fig. 2a are

$$E_e = \left(\frac{\rho}{\rho_0}\right)^{-0.1} \frac{0.09 T_{ekK}^2}{1 + 5\cdot 10^{-4}\, T_{ekK}^2}\,(1 + 1.5\cdot 10^{-5}\, T_{ekK}^{-2.7}),\ \ 10^9[\mathrm{J/m^3}] \tag{10}$$

$$P_e = 1.09\,(\rho/\rho_0)^{0.05}[0.09\, T_{ekK}^2(-At + 0.5) + (1.4\, T_{ekK}^{1.15} - 11)(At + 0.5)] + 0.58259\ \ [\mathrm{GPa}], \tag{11}$$

where $At = \arctan[(T_{ekK} - 13)/2]/\pi$, temperature T_{ekK} is measured in [kK], and the equilibrium density $\rho_0 = 16.69\,\mathrm{g/cm^3}$. Functions (10) and (11) approximate results of DFT calculations. They are used in our 2T hydrodynamics (2T-HD) simulations to trace thermal and hydrodynamic evolution of an irradiated Ta target. Influence of density variations near equilibrium ρ_0 is small for electron temperatures below 5 eV, which is in the range of our interest. But for higher electron temperature, the cohesion effects become weaker than thermal effects when T_e increases above ~ 10 eV. Then, electron energy density E_e and electron pressure P_e significantly increase with increase of density at fixed temperatures T_e, T_i.

2.3 Two-temperature electron heat conduction and electron-ion coupling

Electron-ion coupling parameter α for Ta has been calculated in [34]. The parameter α defines rate of cooling of electron subsystem as result of energy transfer to ions, see heat balance equations (2) and (3). In case of Ta the coupling parameter

$$\alpha(\rho, T_e) \approx 1.27\cdot 10^{17}\,(\rho/\rho_0)\ \ [\mathrm{W/m^3/K}] \tag{12}$$

weakly depends on electron temperature. This is consequence of large width of a d-band, spreading significantly above the Fermi energy level $\mu(T_e = 0)$. In our approximation (12) for Ta, we neglect the T_e -dependence. For aluminum the situation is similar, see Ref. [34, 44–46].

There are significant T_e -dependencies in cases of metals with the upper edge $|\varepsilon_2|$ of a d-band of the order of 1 eV or less [34, 44, 47]. The value ε_2 is measured from Fermi level $\mu(T_e = 0)$. It may be above or below this level. Positive values correspond to transition metals (e.g., Ni), while negative - to noble metals (e.g., Au).

Two-temperature electron heat conduction coefficient has been adopted based on assumptions and calculations done in [34]. In 2T-HD code we use the following approximation

$$f_{lin} = 0.016\, T_{ikK},\ f_{sat} = 0.063,\ a = (f_{lin}^{-2.5} + f_{sat}^{-2.5})^{-0.4},\ \kappa_{low} = T_{ekK}/a,\ \kappa_{high} = 520 + 0.12\,(T_{ekK} + 7)^2,$$

$$\kappa(\rho, T_e, T_i) = (\rho/\rho_0)^3\,(\kappa_{low}^{-1} + \kappa_{high}^{-1})^{-1}\ \ [\mathrm{W/m/K}]. \tag{13}$$

where the electron and ion temperatures T_{ekK}, T_{ikK} are measured in kK, and $\rho_0 = 16.654$ g/cm ^{3}.

3 Experimental setup

Ultrafast imaging interferometry [48] was applied to record expansion dynamics of a sample surface, heated by femtosecond laser pulses, with temporal and spatial resolution. The samples were polycrystalline tantalum films with thickness 0.7-1.4 microns deposited onto glass substrates. The source of femtosecond pulses was a high power Cr:forsterite laser system. This system generates pulses of 80 fs duration at a wavelength of 1240 nm [49]. The laser beam was split into a high-power pump beam and a weaker probe beam. The time interval between the pump and probe pulses was varied by the optical delay line. Probe pulse was a second harmonic with wavelength 620 nm. The p-polarized pump beam at a fundamental wavelength was focused on a surface at an angle of incidence 45 degree in air. Due to oblique illumination, a focal spot at a target surface has elliptical shape with semiaxis ratio which equals to $r_{0x}/r_{0y} = 1/\sin 45^o$. Fluence distribution along a Ta film boundary is $F(x, y) = F_c \exp(-x^2/r_{0x}^2 - y^2/r_{0y}^2)$; $r_{0y} = 42$ microns. The diagnostic part of the setup is based on a Michelson interferometer in imaging configuration. Fourier processing of interference patterns ensured the accuracy of surface displacement at ± 1 nm.

The ablation threshold measured using well known technique [50] for incident fluence was $F_{inc}|_{abl} = 0.31$ J/cm^2. Reflection coefficient of Ta at the ablation threshold and for pump wavelength is $R = 0.38$. The coefficient R, important for quantitative comparisons with simulations, was specially measured in our experiments. This gives value $F_{abs}|_{abl} = (1-R)\,F_{inc}|_{abl} = 190$ mJ/cm^2 for absorbed energy at an ablation threshold. In the experiments the displacement histories $h(t)$ of irradiated surface were measured. The surface velocity profiles $u(t)$ were evaluated by differentiating the measured $h(t)$ dependencies, see below.

4 Separation of compression wave from a heated layer

4.1 Two-temperature thermal and hydrodynamic phenomena

Description of two-temperature relaxation shown in Fig. 4a follows from solution of 2T-HD equations (1-3). Eo2TS (Equation of 2T State) in forms (10) and (11) together with coupling parameter (12) and heat conduction coefficient (13) are used. In Figs. 4 and 5 the absorbed energy is $F_{abs} = 200$ mJ/cm^2, duration of Gaussian pulse is $\tau_L = 100$ fs, thickness of skin-layer is $\delta = 15$ nm. 2T relaxation lasts relatively long time, see Fig. 4**a**. Maximum ion temperature achieved after 2T relaxation is near ≈ 6 kK. It is achieved in time interval 12-16 ps. After 2T relaxation the 1T regime is established, and the maximum on temperature profile begins to decrease with time as a result of heat conduction to the bulk of target having room temperature.

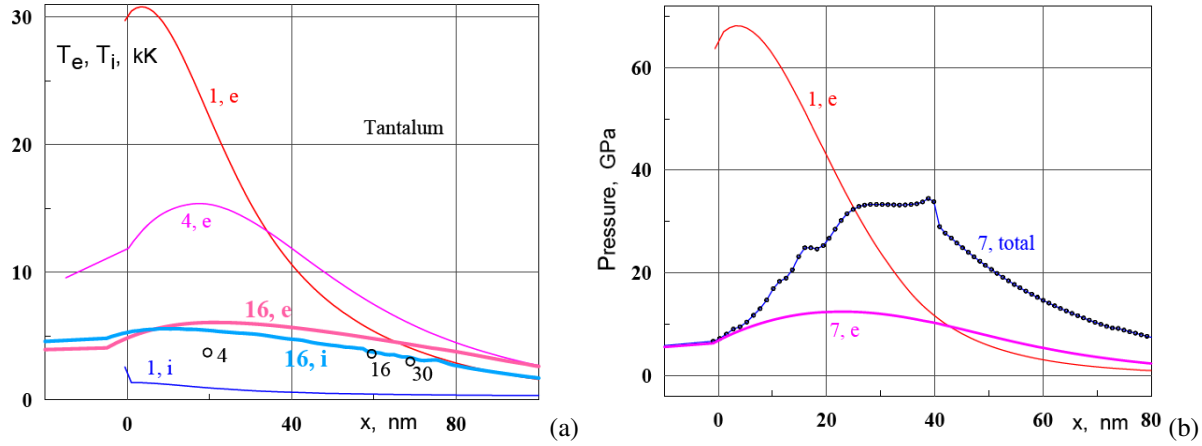

Fig. 4 2T relaxation after action of laser pulse; tantalum, $F_{abs} = 200$ mJ/cm^2, $\tau_L = 100$ fs. (a) Notes near the curves show time instants in ps; e - T_e, i - T_i. Three empty circles correspond to position and temperature T_i at the melting front at time instants 4, 16, and 30 ps. Temperatures T_i at the first two time instants are higher than the triple point temperature 3290 K of Ta, since at those instants melting process takes place under significant external (external relative to the melting zone where the solid-liquid transition locates) pressure, see text. (b) Transition from electron pressure P_e dominated regime at the beginning of 2T stage to the ion pressure P_i dominated regime at the end of 2T stage; $P_e(x, t = 1\text{ ps})|_{max}/P_i(x, t = 1\text{ ps})|_{max} = 15$. Digits near the curves give time instants, e : P_e, total : $P = P_e + P_i$. The chain of small circles show instant positions of a set of Lagrangian particles $x(x^0, t)$ at the (x, p) -plane, see Subsection 2.1 for definition of $x(x^0, t)$.

Propagation of melting front from left side to right is marked in Fig. 4**a** by sequence of three empty circles. We see how the front decelerates by comparing the distances and corresponding time instants between the empty circles. There is a melting zone around the melting front. In this zone solid gradually transfers into liquid through a two-phase solid-liquid phase transition. Pressure at the melting front gradually decreases at acoustic time scale t_s. At the instants 4, 16, and 30 ps, corresponding to the sequence of three empty circles in Fig. 4a, the pressures in the melting zone decrease from 43 GPa to 21 GPa, and then to 0.8 GPa. The maximum of pressure $P_{max}(t)|_{compr}$ in a compression wave passes melting front at $t \approx 11$ ps; $P_{max}(t = 11\text{ ps})|_{compr} \approx 27$ GPa. An acoustic wave gradually develops into combination of a positive pressure wave and negative pressure wave [5, 8, 51–55]. Its amplitude for absorbed fluence $F_{abs} = 200$ mJ/cm^2 is significantly below the bulk modulus of Ta: $K = 200$ GPa. Therefore we speak about a weakly non-linear acoustic wave. The zero pressure value, separating positive and negative parts of an acoustic perturbation, passes through a melting zone at $t \approx 40$ ps. Acoustic time scale is $t_s = d_T/c_s$, where d_T is a thickness of a heated layer, c_s is a speed of sound. Value

$t_s \approx 20$ ps if we take thickness of molten layer $x_m(t)$ at $t = 30$ ps, $x_m(30) \approx 70$ nm and speed of sound $c_s \approx 4$ km/s.

Expansion of target boundary into vacuum is driven by the total pressure $P = P_e + P_i$. During the short 2T stage, main driving pressure in this sum is changed from P_e to P_i, see Fig. 4b. At time instant $t = 1$ ps, ratio of electron to ion pressure is 15. The 2T stage is short in the sense that temperature equilibration time t_{eq} is shorter than acoustic time t_s. System of 2T hydrodynamics equations (1-3) is written in Lagrangian space coordinate x^0. Increment of mass of column per column cross-section area is $dm = \rho^0\, dx^0$ g/cm^2, where ρ^0 is initial density of homogeneous target prior to pulse action.

Instant positions at $t = 7$ ps of Lagrangian particles are shown in Fig. 4b by small circles. The left edge particle is strongly expanded because here pressure drops to vacuum value. Density of Lagrangian particles is too low to follow the evaporation process since physical density contrast between condensed phase and vapor is very high - 3-4 orders of magnitude for the value of absorbed energy corresponding to Figs. 1. We clearly see evaporation in molecular dynamics (MD) simulation described below. Dynamically the evaporation is insignificant in our conditions of very short laser pulse of moderate intensity. Indeed, vapor pressure is many orders of magnitude less than pressures created in condensed matter as result of laser heating. Amount of evaporated mass is very small, thickness of evaporated layer is less than 1 nm [8].

Instant concentration of evaporated atoms decreases from left to right in direction of x-axis in Fig. 4 due to decrease of ion temperature. There is pure vapor to the left from the boundary of the liquid spallation layer. Above ablation threshold there is a foam region (see next Section). It is located between the liquid spallation layer and the continuous bulk of a target. Concentration of evaporated atoms inside bubbles in foam decreases from left to right - from external to internal bubbles.

Fig. 5 shows how a shift $h(t) = -[x(t) - x(-\infty)]$ of Ta boundary and its velocity $\dot{h}(t)$ depend on time. Time is reckoned from the maximum of a pump pulse Q in Eq. (3); trajectory of Ta boundary is $x(t)$. The Lagrangian particles near the left target edge move to the left side in Fig. 4. For the first time, computed and experimental measurements clearly show existence of an acceleration stage. Previously this stage looks like a jump from zero to maximum velocity. The acceleration stage covers time interval from the arrival of pump and up to the maximum of velocity $\dot{h}(t)$. We connect this rather slow acceleration with large density of Ta and rather long 2T stage during which the transition from P_e to P_i drive takes place.

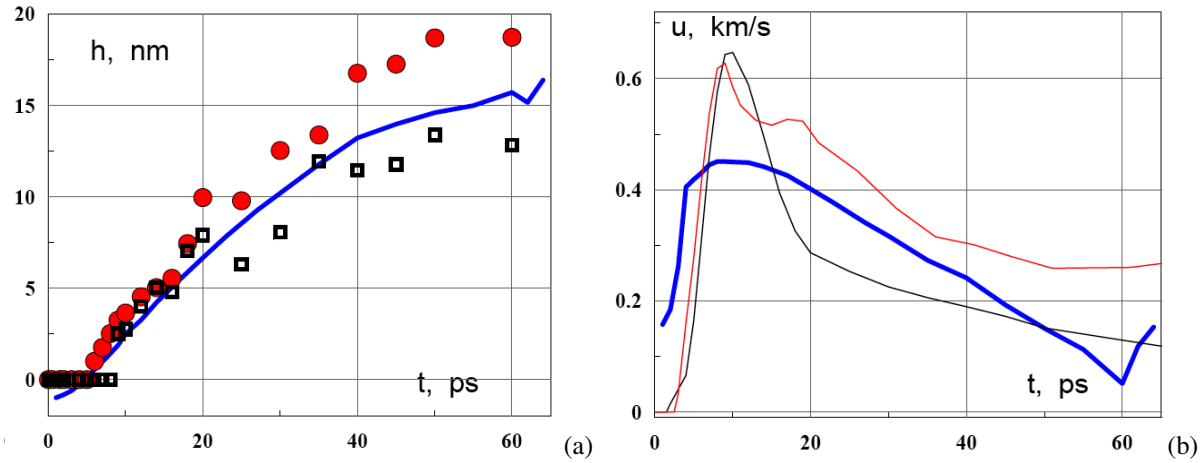

Fig. 5 a) Time-dependent displacement $h(t)$ of Ta boundary into the vacuum side after laser irradiation. 2T-HD simulation shown by solid line, while pump-probe experimental measurements by circles and squares; $F_{abs} = 200$ mJ/cm^2 for 2T-HD (for 2T-HD spatial profiles are shown in Fig. 4), and $F_{abs} = 220$ mJ/cm^2 - circles, $F_{abs} = 180$ mJ/cm^2 - squares. Experimentally measured ablation threshold is $F_{abs}|_{abl} \approx 200$ mJ/cm^2. b) expansion velocities $u(t) = dh(t)/dt$ obtained in 2T-HD (thick blue curve) and from pump-probe measurements: $F_{abs} = 220$ mJ/cm^2 - red curve, $F_{abs} = 180$ mJ/cm^2 - black curve.

4.2 Emission of compression wave during deceleration of supersonic heat wave

Let us consider formation of shock as result of ultrashort laser pulse action. There are absorption of pump pulse, 2T-stage, and acoustic stage. The compression wave is formed during transition from 2T-stage to acoustic stage. 2T-stage is rather long in time, see delay between the times of pump arrival and the velocity maximum in Fig. 5b. There are heat conduction and expansion of a heated layer into bulk of metal, electron heating of ions, and formation of pressurized layer with pressure distribution $P(x;t_{eq})$. It is important that duration of 2T-stage t_{eq} is shorter than acoustic time scale $t_s = d_T/c_s$. There is acoustic decay of pressure distribution $P(x,t_{eq})$ into two $P_- + P_+$ running waves. In linear approximation we have $P_- = (1/2)P(x + c_s t;t_{eq})$, $P_+ = (1/2)P(x - c_s t;t_{eq})$. The left (see definition of left-right directions in Fig. 4) wave P_- is reflected from vacuum boundary $P_-(x) \to P_-(-x)$, changes sign of pressure amplitude $\to -P_-(-x)$, and begins move to right $P_{refl} = -(1/2)P(-x + c_s t;t_{eq})$ in the wake of compression wave P_+. There is approximately double decrease in amplitude of positive pressure during transition from 2T-stage to acoustic stage, see Fig. 6a. After that the maximum pressure $P_{max}(t)$ in a compression wave stays constant in time up to the moment t_2 when the spatial position $x_{max}(t)$ of the maximum $P_{max}(t)$ begins to coincide with position $x_{sw}(t)$ of a shock. Shocks appears at the instant t_{focus} due to non-linear focusing of characteristics. Breaking of Riemann wave takes place before the instant t_2. After the instant t_2 the maximum pressure $P_{max}(t)$ (shock amplitude after t_2) slowly decreases with time since the flow behind a shock is subsonic and rarefaction wave attenuates the shock.

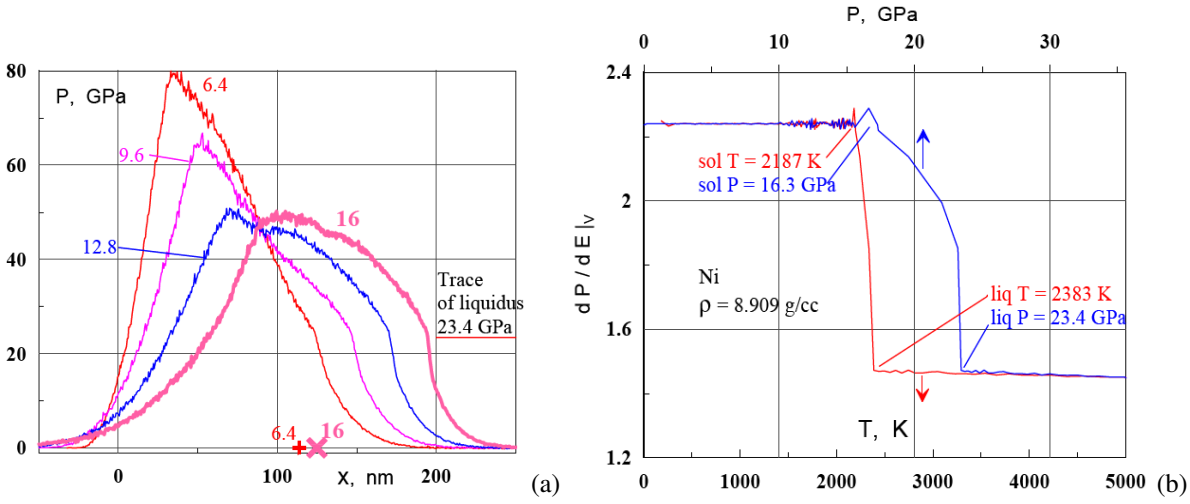

Fig. 6 (a) Formation and acoustic decay of pressure wave in Nickel which absorbs 0.6 J/cm^2 energy. Molecular dynamics simulation; pulse duration is 100 fs. The digits near curves give time instants in ps. The digits near two crosses give time instants in ps. Those crosses show positions of melting front $x_{melt}(t)$. (b) Decrease of "differential" Gruneisen parameter $dp/dE|_V$ during melting. Here a value $dp/dE|_V$ is plotted as a function of temperature T or pressure P along isochoric line $\rho = \rho_0$. Rigidity of matter drops down in two-phase crystal-liquid zone. This zone is separated from solid by solidus and from liquid by liquidus. The solidus and liquidus are selected by notes "sol" and "liq".

The pressure profiles in Fig. 6a shifts to the right side with velocity ≈ 7.1 km/s. This propagation velocity is significantly above elastic speed of sound $c_{elast} \approx 6$ km/s in Ni. In usual conditions the speed of propagation of elastic compression wave deviates from speed c_{elast} slightly, not more than 50-100 m/s. Above this limit, the elastic wave in usual conditions is accompanied by plastic shock. In our molecular dynamics simulation, the solid Ni locates at the right side relative to melting front $x_{melt}(t)$ shown by the crosses in Fig. 6a. This remains in elastic uniaxial compression state. No plastic transformations take place in spite of huge values of shear stresses.

In Fig. 6b dependencies along the particular isochoric line $\rho = \rho_0$ are shown. Density for this isochoric line corresponds to equilibrium density ρ_0 of Ni. Rigidity of Ni decreases when the isochoric line intersects a melting curve. Figuratively speaking, two continuous parts and one steep part of dependencies shown in Fig. 6b resemble a binodal curve at the ρ, T phase plane. The steep part corresponds to the interval of the triple point. The steep decrease of rigidity of matter leaves a trace in profiles of propagating compression wave shown in Fig.

6a. We see that a pressure profile is steeper below the point marked by the horizontal straight line in Fig. 6a. This straight line corresponds to pressure in the intersection point of the curve of liquidus and the isochoric curve at the ρ, T or ρ, P planes of thermodynamic phase space, see also Fig. 6b. The steeping of the pressure profile appears at the supersonic melting stage. After transonic deceleration of heat wave, the steepening is carried along the characteristics lines together with the value of pressure in the intersection point.

Significant rise in the steeping is the reason of formation of elastic shock with pressure amplitude which equals to the value of pressure in the liquidus/isochoric intersection point. This interesting feature has been marked in our previous papers [56, 57]. Results in those papers have been based on 2T-HD simulations. Here we found an initial amplitude of elastic shock from MD simulations, see also [12]. Let us emphasize that in the 2T-HD simulations both kinks, corresponding to solidus and liquidus, are seen. In molecular dynamics only the upper kink is seen. As was said above, it refers to the liquidus.

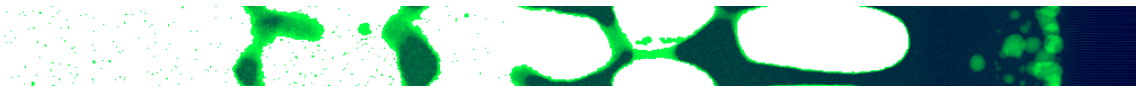

Fig. 7 Distribution of matter involved in flow after action of ultrashort laser pulse. Parameter of pulse are $F_{abs} = 270$ mJ/cm^2, $\tau_L = 100$ fs. This is MD simulation of freestanding tantalum film. EAM Johnson potential has been used to describe atom-atom interactions. Initial data are taken in accordance with 2T-HD results for this particular laser pulse. We define the bottom as the plane $x = x_{bott}(t)$ at the right side where the largest bubbles end. The x-axis is directed from left to right as in Figs. 4. Ratio of vertical and horizontal scales is 1:1. Vertical (y-direction) height is 24 nm. Cross section $y \times z$ of box is 24×12 in nanometers. We see interesting phenomenon of secondary nucleation exactly near the melting-recrystallization front. Crystal is at the right side from this front. Molten tantalum is at the left side from the front. Instant 188 ps after arrival of pump pulse is shown. Secondary nucleation takes place as result of action of tensile stress wave. This wave appears after reflection of compression wave from the rear-side boundary of a film. Thickness of film is 400 nm. The rear-side boundary is the right side end of the film. It is located more to the right than the shown frame.

5 Foaming and freezing

Quickness and smallness (very small depth is heated) of femtosecond pulse is a reason of interesting physical phenomena: super-elasticity of solids, approaching ultimate strength against elastic-plastic transformation [16–24], and nanospallation of liquid layer, where surface tension of bubble foam becomes dynamically significant [8, 29, 31–33]. Spallation of liquid nanolayer with thickness comparable to skin depth δ (Subsection 2.1) is a reason for appearance of interference Newton rings [28–30, 58, 59] since so thin layer of molten metal or semiconductor is transparent for probe laser light. Never before spallation layer was so thin to be transparent.

Another unusual physical situation is described in this Section. As a rule, hydrodynamics and solidification are separated due to quickness of hydrodynamics and slowness of solidification. It is difficult to imagine a fountain water jet crystallized in its fly. Formation of icicles is mainly thermal process, if we think about fountain hydrodynamics. Of course, gravity drain of water is significant ingredient of icicles growth. Below we describe nanojets solidified in their flight.

Let's consider this phenomena. Absorbed fluence F_{abs} is the main parameter controlling results of femtosecond action. Below a melting threshold $F_{abs}|_{melt}$ irradiated target remain solid. Between thresholds $F_{abs}|_{melt}$ and $F_{abs}|_{nucl}$ a layer of molten metal keeps its continuity (no nucleation). At a nucleation threshold $F_{abs}|_{nucl}$ first viable nuclei appears. It is important that nucleation takes place appreciably below ablation: $F_{abs}|_{abl} - F_{abs}|_{nucl} \sim 0.1\, F_{abs}|_{abl}$ [31–33]. This is also the consequence of quickness and smallness; in the less quick process the relative gap $(F_{abs}|_{abl} - F_{abs}|_{nucl})/F_{abs}|_{abl}$ between nucleation and ablation thresholds is smaller. There is no separation of matter in the form of spallation layer in the interval $F_{abs}|_{nucl} < F_{abs} < F_{abs}|_{abl}$. After femtosecond action a metal surface moves into vacuum side and undersurface bubbles grow, but in this interval of values F_{abs}, a surface tension stops spallation layer in its motion away. After this stop the velocity of boundary changes sign as result of reduction of undersurface bubbles in size. There is a competition between processes of the bubble collapse from one hand and solidification of liquid around a bubble from another hand. Often the solidification wins this competition. In this case bubbles remain under surface in solid matrix around [31–33].

There is an evaporation threshold $F_{abs}|_{ev} \sim 1.4\,F_{abs}|_{abl}$ for Ta. There is a liquid spallation layer in the interval $F|_{abl} < F < F|_{ev}$ between those two thresholds [8, 53]. From left to right along x -axis (see Figs. 4 for definition of direction), in this interval, the ejecta in a plume has following structure: (i) vapor, (ii) spallation layer, (iii) vapor-liquid mixture, (iv) crater bottom, and (v) the rest of a target. Above threshold $F_{abs}|_{ev}$ the second link in this chain disappears. At even higher fluences F_{abs}, vapor becomes hotter and expands faster. This increases a difference between hot vapor in the head of plume and two-phase mixture near the crater bottom, since parameters of two-phase mixture near the bottom do not depend significantly on absorbed fluence. At the instant picture of a developed plume, the bottom bubbles are larger in their sizes than bubbles in the mixture more far from the bottom, see Fig. 7. Hot vapor and hot vapor-droplet mixture move fast, while velocities of liquid films in the bottom part of a plume are low $\sim 10 - 100$ m/s. Liquid films form approximately flat segments separating neighbor bubbles in a foam.

The left, middle and the bottom parts of a tantalum plume are presented in Fig. 7. Laser pump pulse comes from the left side. Instant density map is shown in Fig. 7. Fast hot pure vapor moves first. The more to the left, the hotter vapor is. The smallest dots in Fig. 7 correspond to evaporated atoms. Evaporated atoms are presented in vapor, in foam, and inside bubbles. Temperature and atomic concentration of vapor drop down from left to right. Gradually from left to right the pure vapor transfers to the vapor-droplet mixture. Sizes of droplets increase to the right. First, small clusters of atoms appear in vapor environment. At our time scale the droplets appear as result of expansion and disintegration of foam type vapor-liquid mixture, while the smallest clusters may be result of evaporation. Expansion of mixture and inflation of particular bubble are connected with x -velocity gradient. Much later in time droplets begin to evaporate, while vapor slowly condenses into small droplets [6, 60, 61].

Evolution of small size bubble ensemble near the melting-recrystallization front is shown in Figs. 8. Let us discuss why a cavitation rather late in time (much later than acoustic time scale $t_s = d_T/c_s \approx 20$ ps) and exactly at liquid-solid phase boundary appears. Formation of compression wave in 2T-HD and in MD simulations is shown in Figs. 4b and 6fa. The wave propagates to the right. In case of film the wave achieves a rear-side of a film. Compression wave reflects as a tensile wave from the rear-side vacuum boundary. This tensile wave propagates back from the right side to the left side. Amplitude of the tensile wave, when it arrives to the phase separation front, depends on absorbed fluence F_{abs} (larger F - then larger amplitude) and thickness of a film d (larger d - smaller amplitude). In our case ($F_{abs} = 270$ mJ/cm^2, $d = 400$ nm) this amplitude is not enough to cause spallation in solid tantalum. But it is enough to cause cavitation in liquid, since strength of liquid is significantly smaller than strength of solid see Fig. 8 in [16] and [62]. The tensile wave comes from the solid side. Therefore it nucleates liquid near the melting-recrystallization front if its amplitude hits into the gap between the maximum liquid strength and solid strength.

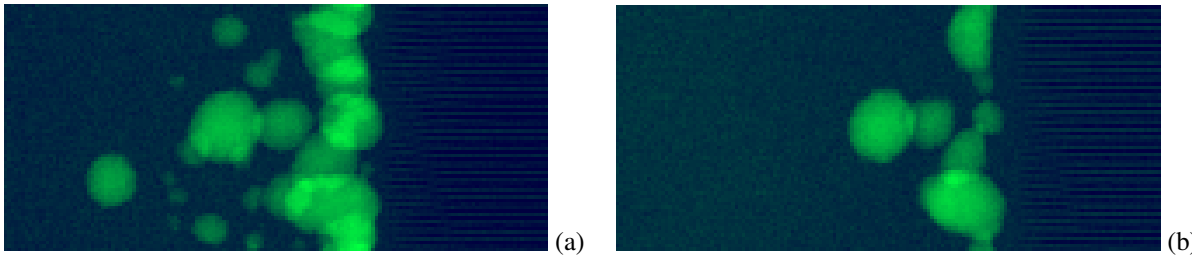
(a) (b)

Fig. 8 Appearance and decay of cavitation near the liquid-solid phase boundary. During decay sizes and number of bubbles decrease. Let us attract reader attention to the unusual shapes of bubbles. Some of them are "sitting" at the phase boundary. In this case part of their surrounding surface is liquid and part is solid. The solid part is approximately flat. Therefore bubbles take beautiful hemispherical (snap) shape. (a) $t = 188$ ps. (b) $t = 199$ ps. The upper bubble has shape of a hemisphere.

There are primary and secondary cavitations. Primary liquid nucleates at acoustic time scale $t_s = d_T/c_s \sim 10 - 20$ ps, where d_T is thickness of heated layer. Secondary nucleation appears much later. Indeed, pressure wave has to pass twice thickness of a film $\sim 2\,(d - d_T)/c_s$. This situation is similar to the situation discussed in paper [16], where aluminum film was deposited onto glass plate surface. Pump irradiates glass-aluminum surface through glass. Irradiation, firstly, forms molten layer near glass-aluminum boundary and, secondly, it produces compression wave which returns back to the molten layer after reflection from the rear-side. This reflected tensile

wave does not spalled solid, but it causes cavitation when it arrives into liquid. The difference with considered in Figs. 7 and 8 case is that here [16] we don't have a glass supporting metal against primary cavitation.

Let us pay attention also to the hemispherical bubbles dissected by solid-liquid interface, see Fig. 8b. Deformation of bubbles during their freezing has been described in [33]. But in this work the recrystallization front comes from one side of the bubbles and begins to freeze them. While here (Figs. 7 and 8) the bubbles from their beginning appear at the solid-liquid interface. Another point concerns interesting observations. The secondary cavitation may give explanation to the mysterious phenomenon observed in our recent experiments (unpublished). In experiments with tantalum films, above certain threshold $F_{abs}|_2 \approx 2.5\, F_{abs}|_{abl}$ higher than the ablation threshold $F_{abs}|_{abl}$ two craters pattern has been found (one crater is inside another one). First crater appears at the ablation threshold and has depth $h_1 \approx 20 - 30$ nm. At the rather sharp threshold F_2 the second crater is formed inside the first one. Its depth at the threshold F_2 is $h_2 \approx 70 - 80$ nm. The depths h_1 and h_2 are close to the depths of primary and secondary cavitations shown in Figs. 7 and 8. Unfortunately, the secondary solid-liquid cavitation in our series of simulations finishes with collapse of secondary bubbles. Also for simulation shown in Figs. 7 and 8 the ratio of thresholds F_2/F_{abl} is smaller than 2.5. But thickness of film 0.4 micron in Figs. 7, 8 is smaller than thickness in experiment 1.4 micron. This fact decreases the ratio F_2/F_{abl}.

Above processes of nucleation, expansion of vapor-liquid mixture, formation of foam, and expansion of foam have been studied. We see that the bottom part of a foam expands slowly, velocities here are low ~ 10 m/s. The bottom part of foam locates near the bottom of the future crater. At so small velocities, long times (hundreds and thousands picoseconds) are necessary to mechanically disintegrate liquid walls forming foam. During disintegration there is a transit from integrated foam to vapor-droplet mixture. At such long times cooling by electron heat conduction becomes important. Conduction loses into bulk lead to cooling and solidification of molten metal.

Competition between dynamical breaking of internal ties of foam (from one side) and freezing of foam (from the other side) defines late time evolution in the bottom part of a foam. Internal ties form dynamically integrated interconnected structure. Namely this structure resists to stretching of foam. Foam is poor heat conductor. Therefore spallation plate fly away in state of hot molten metal. But the bottom part of a foam loses heat as result of cooling into bulk. Gradually liquid walls forming foam begin solidify. The process of crystallization of liquid walls in motion is shown in Fig. 9.

An aluminum film shown in Fig. 9 has initial spatial dimensions $500 \times 240 \times 24$ nm^3; 172 million atoms. Absorbed fluence $F_{abs} = 120$ mJ/cm^2 is above ablation threshold by 45%. Strong foaming takes place at this fluence enlarged in comparison with ablation threshold, see Fig. 9a. Stretching of liquid walls separating foam cells leads to decrease of thickness of wall and to decrease of mass per unit of wall surface. Particular wall breaks when its thickness drops down to few interatomic distances. Walls are stretched and therefore they exist in stressed state. Breaking a small hole through the particular wall segment leads to fast expansion of hole. As result this segment disappears and two neighbor cells unify. Neighboring walls dynamically compete with each order. Thinner walls expand faster and disappear.

Very important feature used in MD code is that it includes Monte-Carlo model of electron heat conduction. Electron heat conductivity of metals is much larger than ion heat conductivity, therefore pure MD simulation underestimates substantially the heat propagation in metals at nanoscales, where large temperature gradients are generated by femtosecond laser irradiation. MD combined with Monte-Carlo approach for electron thermal transport has significant advantage over common MD coupled with 1D continuous heat equation - it allows to determine accurately the heat flux through such topologically complicated region as a foam, where heat is transported along branching walls. Green and red colors in Figs. 9b-e separates crystalline metal and melt. Simulations show that at late stages liquid is overcooled, since solidification velocity is limited by a value which is few times below velocity $u_{recryst} = \Delta q/\rho\lambda$ in Stefan problem. Here Δq is a heat flux jump at a front, λ is heat of fusion per unit mass. In those overcooled conditions the nuclei of new crystalline phase appears outside of the crystallization front - at free surface of bubbles and even inside bulk melt, see Fig. 9c. Those nuclei are clearly seen as green spots inside red molten aluminum. Stage of growth of such nuclei inside liquid finishes with formation of polycrystalline solid with nanoscale crystallites. They form a crust between bottom of a foam and bulk metal, see Figs. 9d,e. Evolution of mobile dislocations in thermally stressed solid near recrystallization front is also interesting. Dislocations define motions of spots with tints of green color in crystal under solidification front in Figs. 9b-e.

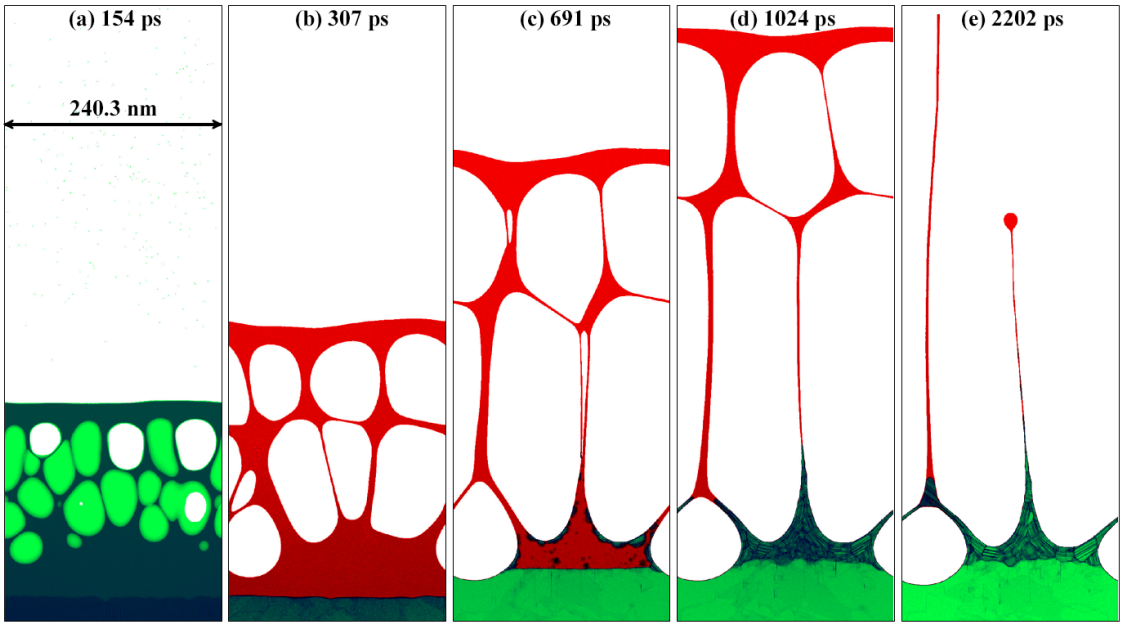

Fig. 9 Expansion and freezing of foamed aluminum. As a result of electron cooling of molten surface layer the re-solidification front moves up through continuous melt and reaches the bottoms of bubbles. Due to supercooling of surface liquid at later time, solid nuclei are also formed inside the melt and at free surface. (a) cavitation in liquid surface layer shown on density map; (b-e) atomic order parameter shows phase state of material: green colors correspond to solid state, while red colors correspond to liquid; (c) crystallization begins at liquid-solid interface first, then in bulk of supercooled melt and at free boundary of melt; (d) crystallization of foam walls initiated by formation of solid nuclei on free liquid surfaces of walls; (e) liquid walls are broken, a tiny droplet forms at the end, and liquid jet moves back to the target along partially frozen pike.

6 Conclusion

The reasons for formation of complex nanostructures on irradiated metal surface were revealed in this paper for the first time. The main reason is found to be decay of a metal foam resulting in formation of liquid structures like threads/pikes, followed by freezing of those structures. It gives us insight into the physical mechanism leading to a characteristic scale of frozen surface structures, which is of the order of heated depth $d_T \sim 100$ nm produced by heat propagation during electron-ion thermalization stage. The mechanism of nano-structuring is composed of sequence of processes starting from void nucleation in a stretched melt, which is followed by rapid cavitation and expansion of foam-like melt, breaking of foam, and subsequent recrystallization of surface and freezing of foam remnants.

By contrast with theories of interference between incident wave and surface plasmons used to explain appearance of LIPSS (laser induced periodic surface structures), which predict the surface structure scale of the order of wavelength ~ 1 micron typical for electromagnetic waves in optical range, our results give much smaller structure scale of the order of heated depth 100 nm. We think that a future complete theory of surface nanostructuring should include both thermomechanical processes and surface interference as well as interplay between them.

Acknowledgements The work of N.A.I., Yu.V.P., V.A.Kh., S.I.Ash., K.P.M., V.V.Sh., and M.B.A. was supported by the Russian Foundation for Basic Research (project no. 13-08-01095). The work of V.V.Z and I.I.O. was supported by the National Science Foundation under Grant No. DMR-1008676. MD simulations were performed using NSF XSEDE facilities Stampede and Kraken. Authors are grateful to A.E. Mukhanov (FSUE VNIIA) for his help with DFT calculations. The work of K.V.Kh. was also supported by the Russian Foundation for Basic Research (project nos. 11-08-01225, 13-02-91057, and 13-08-12248).

References

[1] S.I. Anisimov, B. Kapeliovich, and T. Perel'man, Sov. Phys. JETP **39**, 375–377 (1974).
[2] R. Pakula and R. Sigel, Physics of Fluids **28**(1), 232–244 (1985).
[3] Y. Afanasiev, B. Chichkov, N. Demchenko, V. Isakov, A. Kanavin, S. Uryupin, and I. Zavestovskaya, Proc. SPIE **3885**, 232–244 (2000).
[4] K. Eidmann, J. Meyer-ter-Vehn, T. Schlegel, and S. Hueller, Rhys. Rev. E **62**, 1202–1214 (2000).
[5] D.S. Ivanov and L.V. Zhigilei, Phys. Rev. B **68**(Aug), 064114 (2003).
[6] S. Amoruso, R. Bruzzese, X. Wang, and P. Atanasov, J. Phys. D.: Appl. Phys. **40**, 331–340 (2007).
[7] M. Povarnitsyn, T. Itina, M. Sentis, K. Khishchenko, and P. Levashov, Phys. Rev. B **75**, 235414 (2007).
[8] N.A. Inogamov, V.V. Zhakhovskii, S.I. Ashitkov, Y.V. Petrov, M.B. Agranat, S.I. Anisimov, K. Nishihara, and V.E. Fortov, JETP **107**, 1–19 (2008).
[9] M. Gill-Comeau and L. Lewis, Phys. Rev. B **84**, 224110 (2011).
[10] A. Mayer, K. Khishchenko, P. Levashov, and P. Mayer, J. Appl. Phys. **113**, 193508 (2013).
[11] B. Demaske, V. Zhakhovsky, N. Inogamov, and I. Oleynik, Phys. Rev. B **82**, 064113 (2010).
[12] B.J. Demaske, V.V. Zhakhovsky, N.A. Inogamov, and I.I. Oleynik, Phys. Rev. B **87**(5), 054109 1–9 (2013).
[13] A. Volkov and L. Zhigilei, J. Phys.: Conf. Ser. **59**, 640–645 (2007).
[14] N.A. Inogamov, V.V. Zhakhovskii, S.I. Ashitkov, V.A. Khokhlov, Y.V. Petrov, P.S. Komarov, M.B. Agranat, S.I. Anisimov, and K. Nishihara, Applied Surface Science **255**, 9712–9716 (2009).
[15] V. Zhakhovskii, N. Inogamov, Y. Petrov, S. Ashitkov, and K. Nishihara, Applied Surface Science **255**, 9592–9596 (2009).
[16] M. Agranat, S.I Anisimov, S. Ashitkov, V. Zhakhovskii, N. Inogamov, P. Komarov, A. Ovchinnikov, V. Fortov, V. Khokhlov, and V. Shepelev, JETP Letters **91**, 471–477 (2010).
[17] V.V. Zhakhovskii and N.A. Inogamov, JETP Lett. **92**, 521–526 (2010).
[18] S. Ashitkov, M. Agranat, G. Kanel', P. Komarov, and V. Fortov, JETP Letters **92**, 516–520 (2010).
[19] V.V. Zhakhovsky, M.M. Budzevich, N.A. Inogamov, I.I. Oleynik, and C.T. White, Phys. Rev. Lett. **107**(13), 135502 (4) (2011).
[20] N. Inogamov, V. Zhakhovskii, V.A. Khokhlov, and V. Shepelev, JETP Letters **93**(4), 226–232 (2011).
[21] V.H. Whitley, S.D. McGrane, D.E. Eakins, C.A. Bolme, D.S. Moore, and J.F. Bingert, J. Appl. Phys. **109**, 013505 (2011).
[22] J.C. Crowhurst, M.R. Armstrong, K.B. Knight, J.M. Zaug, and E.M. Behymer, Phys. Rev. Lett. **107**(Sep), 144302 (2011).
[23] N.A. Inogamov, V.A. Khokhlov, Y.V. Petrov, S.I. Anisimov, V.V. Zhakhovsky, B.J. Demaske, I.I. Oleynik, C.T. White, S.I. Ashitkov, K.V. Khishchenko, M.B. Agranat, and V.E. Fortov, AIP Conference Proceedings **1426**, 909–912 (2012).
[24] V. Zhakhovsky, B. Demaske, N. Inogamov, V. Khokhlov, S. Ashitkov, M. Agranat, and I. Oleynik, AIP Conference Proceedings **1464**, 102–112 (2012).
[25] S.A. Abrosimov, A.P. Bazhulin, V.V. Voronov, I.K. Krasyuk, P.P. Pashinin, A.Yu. Semenov, I.A. Stuchebryukhov, K.V. Khishchenko, Doklady Physics **57**, 64–66 (2012).
[26] S.A. Abrosimov, A.P. Bazhulin, V.V. Voronov, A.A. Geras'kin, I.K. Krasyuk, P.P. Pashinin, A.Yu. Semenov, I.A. Stuchebryukhov, K.V. Khishchenko, and V.E. Fortov, Quantum Electron **43**, 246–251 (2013).
[27] N. Inogamov, Y. Petrov, V. Zhakhovsky, V. Khokhlov, B. Demaske, S. Ashitkov, K. Khishchenko, K. Migdal, M. Agranat, S. Anisimov, and V. Fortov, AIP Conference Proceedings **1464**, 593–608 (2012).
[28] N.A. Inogamov, Y.V. Petrov, S.I. Anisimov, A.M. Oparin, N.V. Shaposhnikov, D. vonder Linde, and J. Meyer-ter-Vehn, JETP Letters **69**, 310–316 (1999).
[29] V. Zhakhovskii, K. Nishihara, S. Anisimov, and N.A. Inogamov, JETP Lett. **71**, 167–172 (2000).
[30] S. Anisimov, V. Zhakhovskii, N. Inogamov, and et al., JETP Lett. **77**, 606–610 (2003).
[31] V.V. Zhakhovskii, N.A. Inogamov, and K. Nishihara, JETP Letters **87**, 423–427 (2008).
[32] V.V. Zhakhovskii, N.A. Inogamov, and K. Nishihara, J. Phys.: Conf. Ser. **112**, 042080 (2008).
[33] S. Ashitkov, N. Inogamov, V. Zhakhovsky, Y. Emirov, M. Agranat, I. Oleinik, S. Anisimov, and V. Fortov, JETP Lett. **95**, 176–181 (2012).
[34] Y.V. Petrov, N.A. Inogamov, and K.P. Migdal, JETP Lett. **97**, 20–27 (2013).
[35] S. Khakshouri, D. Alfe, and D.M. Duffy, Phys. Rev. B **78**, 224304 (2008).
[36] G.V. Sin'ko, N.A. Smirnov, A.A. Ovechkin, P.R. Levashov, and K.V. Khishchenko, High Energy Density Physics **9**, 309–314 (2013).
[37] P.R. Levashov, G.V. Sin'ko, N.A. Smirnov, D.V. Minakov, O.P. Shemyakin, and K.V. Khishchenko, J. Phys.: Cond. Matt. **22**, 505501 (2010).
[38] X.W. Zhou, R.A. Johnson, and H.N.G. Wadley, Phys. Rev. B **69**(Apr), 144113 (2004).
[39] Shock wave database: http://teos.ficp.ac.ru/rusbank/.
[40] V. Recoules, J. Clerouin, G. Zerah, P.M. Anglade, and S. Mazevet, Phys. Rev. Lett. **96**, 055503 (2006).
[41] V. Stegailov, Contrib. Plasma Phys. **50**, 31–34 (2010).
[42] E. Zijlstra, A. Kalitsov, T. Zier, and M. Garcia, Phys. Rev. X **3**, 011005 (2013).

[43] G.E. Norman, S.V. Starikov, V.V. Stegailov, I.M. Saitov, and P.A. Zhilyaev, Contrib. Plasma Phys. **53**, 129–139 (2013).
[44] Z. Lin, L.V. Zhigilei, and V. Celli, Phys. Rev. B **77**, 075133 (2008).
[45] Y.V. Petrov, Laser and Particle Beams **23**, 283–289 (2005).
[46] B. Rethfeld, A. Kaiser, M. Vicanek, and G. Simon, Phys. Rev. B **65**, 214303 (2002).
[47] X.Y. Wang, D.M. Riffe, Y.S. Lee, and M.C. Downer, Phys. Rev. B **50**, 8016 (1994).
[48] M.B. Agranat, N.E. Andreev, S.I. Ashitkov, M.E. Veisman, P.R. Levashov, A.V. Ovchinnikov, D.S. Sitnikov, V.E. Fortov, and K.V. Khishchenko, JETP Lett. **85**, 271–276 (2007).
[49] M.B. Agranat, S.I. Ashitkov, A.A. Ivanov, A.V. Konyashchenko, A.V. Ovchinnikov, and V.E. Fortov, Quantum Electronics **34**, 506–508 (2004).
[50] J.M. Liu, Opt. Lett. **7**, 196–198 (1982).
[51] S. Anisimov, N. Inogamov, Y. Petrov, V. Khokhlov, V. Zhakhovskii, K. Nishihara, M. Agranat, S. Ashitkov, and P. Komarov, Appl. Phys. A **92**(4), 797–801 (2008).
[52] S. Anisimov, V. Zhakhovskii, N. Inogamov, K. Nishihara, Y. Petrov, and V.A. Khokhlov, J. Experim. Theor. Phys. (JETP) **103**, 183–197 (2006).
[53] M.B. Agranat, S.I. Anisimov, S.I. Ashitkov, V.V. Zhakhovskii, N.A. Inogamov, K. Nishihara, Y.V. Petrov, V.E. Fortov, and V.A. Khokhlov, Appl. Surf. Sci. **253**, 6276–6282 (2007).
[54] N.A. Inogamov, S.I. Anisimov, Y.V. Petrov, V.A. Khokhlov, V.V. Zhakhovskii, K. Nishihara, M.B. Agranat, S.I. Ashitkov, and P.S. Komarov, Proc. SPIE **7005**, 70052F (2008).
[55] S. Anisimov, N. Inogamov, Y. Petrov, V. Khokhlov, V. Zhakhovskii, K. Nishihara, M. Agranat, S. Ashitkov, and P. Komarov, Appl. Phys. A . **92**(4), 939–943 (2008).
[56] N. Inogamov, S. Ashitkov, V. Zhakhovsky, V. Shepelev, V. Khokhlov, P. Komarov, M. Agranat, S. Anisimov, and V. Fortov, Appl. Phys. A **101**, 1–5 (2010).
[57] N. Inogamov, V. Zhakhovsky, S. Ashitkov, V. Khokhlov, V. Shepelev, P. Komarov, A. Ovchinnikov, D. Sitnikov, Y. Petrov, M. Agranat, S. Anisimov, and V. Fortov, Contributions to Plasma Physics **51**(4), 367–374 (2011).
[58] K. Sokolowski-Tinten, J. Bialkowski, A. Cavalleri, D. vonder Linde, A. Oparin, J.M. ter Vehn, and S.I. Anisimov, Phys. Rev. Lett. **81**, 224 (1998).
[59] D. vonder Linde and K. Sokolowski-Tinten, Applied Surface Science **154-155**, 1 (2000).
[60] S.I. Anisimov and B. Luk'yanchuk, Physics-Uspechi **45**, 293–324 (2002).
[61] S. Sonntag, C.T. Paredes, J. Roth, and H.R. Trebin, Appl. Phys. A **104**, 559–565 (2011).
[62] S. Ashitkov, N. Inogamov, P. Komarov, V. Zhakhovsky, I. Oleynik, M. Agranat, G. Kanel, and V. Fortov, AIP Conference Proceedings **1464**, 120–125 (2012).

